Chapter 2

Metamaterial-based Polarization-insensitive Wide-angle Dual-band Microwave Absorber

2.1 Introduction

Conventional microwave absorbers [Salisbury (1952), Fante and McCormack (1988), Naito and Suetake (1971), Toit (1994), Sugimoto *et al.* (1999), Park *et al.* (2000)] need to be replaced in the applications that require lightweight, low profile and low-cost absorbing materials. Such applications include mutual coupling reduction in antenna arrays (discussed in section 1.4 of the previous chapter), radar cross section reduction [Zhang *et al.* (2014)], stealth technology [Iwaszczuk *et al.* (2012)], electromagnetic compatibility [Li *et al.* (2015)], sensors [Liu *et al.* (2010)a], thermal emitter [Liu *et al.* (2011)b], spectroscopy and imaging [He *et al.* (2011)], microwave-to-infrared signature control [Jiang *et al.* (2011)b], and many more. The requirement of having the alternatives of conventional microwave absorbers led to the development of electromagnetically engineered absorbers popularly known as metamaterial absorber. Metamaterial absorbers suitably fit in these applications with the added advantage of frequency tunability over a wide frequency range by just varying the design parameters. Polarization-insensitive nature and wide-angle performance are the desired characteristics of such absorber structures.

Several metamaterial absorber structures with near unity absorption in the upper GHz frequency range to terahertz and infrared frequency ranges are presented in the literature [Landy *et al.* (2008), Wen *et al.* (2009), Cheng and Yang (2010), Zhu *et al.* (2010), Tao *et al.* (2010), He *et al.* (2011), Pitchappa *et al.* (2014), and Wang *et al.* (2015)]. Designing the structure with the small footprint for low GHz frequency range

puts a challenge [Cao *et al.* (2014)]. Recently, the main emphasis is given to the design of compact, ultrathin and multi/wideband structures with near unity absorption.

In this chapter, an ultra-thin wide-angle polarization-insensitive metamaterial unit cell is proposed to achieve dual-band absorbance in the microwave frequency domain. Two distinct absorption frequencies one each in C- and X-band are obtained by suitably combining the basic geometries of the closed ring resonator and the patch in a single unit cell. Identical absorption characteristics for TE and TM polarized incident wave is obtained due to the four-fold symmetry present in the structure. The design schematic and its absorption response are presented in section 2.2. The dependence of the absorption frequency and absorption level on the shape parameters of the proposed structure are discussed in detail in section 2.3. Absorption mechanism of the proposed absorber is discussed with the help of *E*-field and surface current distribution plots in section 2.4. Polarization-insensitive behavior of the proposed absorber is presented in section 2.5. In section 2.6, the electromagnetic parameters of the proposed structure are retrieved using electric and magnetic susceptibilities. A prototype of the proposed absorber is fabricated and is experimentally verified for normal and oblique incident wave in section 2.7 by free space measurement method. Performance comparison of the proposed absorber is provided in section 2.8 with some other dual-band absorber structures reported in the literature in terms of the relative bandwidth, unit cell periodicity and thickness. Section 2.9 finally concludes the presented chapter.

2.2 Design Schematic and Simulated Response

2.2.1 Unit Cell Structure

The unit cell of the proposed absorber is a three-layered structure. The top layer consists of frequency selective surface (FSS) as an electric resonator, the second layer is of FR4 dielectric ($\varepsilon_r = 4.4, \tan\delta = 0.02$) with thickness t = 0.8 mm, and the complete metallic

plane is utilized as the third layer. FSS and the metallic plane are made up of 35 µm thick copper with the finite conductivity of 5.8 x 10^7 S/m. The geometry of the electric resonator is presented in Figure 2.1 along with detailed dimensions. The electric resonator consists of a square-shaped ring resonator with a square patch enclosed in it and the two are connected by the diagonal strips. The optimization of the shape parameters adjust the corresponding inductances and capacitances, and hence the absorption frequency. Since capacitance in the structure also depends on the substrate permittivity and thickness, therefore, these parameters also affect the absorption frequency. The level of absorption is determined by the ohmic loss provided by the resonator resistance and the dielectric loss which mainly depend on the dielectric loss tangent and thickness of the dielectric material [Pang *et al.* (2013)]. The unit cell of the proposed absorber is placed in *xy*-plane, and is analyzed using periodic boundary conditions along *x*- and *y*-direction in CST Microwave Studio. Plane wave modes (TE(0, 0) and TM(0, 0)) are injected into the proposed unit cell from *z*-direction using floquet port excitation in the numerical solver. In TE(0, 0) mode, *E*-field is polarized along *y*-axis while the orientation of *E*-field is along the *x*-axis in TM(0, 0) mode. The optimized parameters of the unit cell are as: p = 12 mm, g_1 = 0.2 mm, w_d = 0.2 mm, l_p = 6 mm, w_c = 0.3 mm.

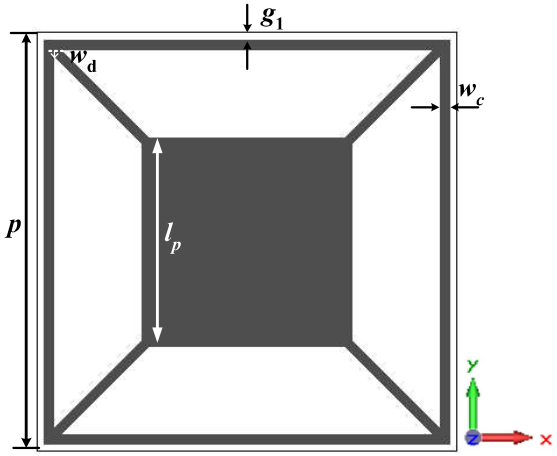

Figure 2.1: Top view of the unit cell of the proposed absorber structure.

2.2.2 Absorption/Reflection Characteristics

Absorption response of such a structure depends on the reflectance $R(\omega)$ and transmittance $T(\omega)$ of the structure as given in Equation 2.1.

$$A(\omega) = 1 - R(\omega) - T(\omega) \tag{2.1}$$

where $R(\omega) = |S_{11}(\omega)|^2$ and $T(\omega) = |S_{21}(\omega)|^2$, $S_{11}(\omega)$ and $S_{21}(\omega)$ denotes the reflection and transmission coefficient of the structure, respectively (1 and 2 denote the ports above the top metallic layer and below the metallic backplane, respectively). The presence of complete metallic backplane reduces the transmittivity ($|S_{21}(\omega)|^2$) of the structure to zero. The absorption of the structure is then calculated using Equation 2.2.

$$A(\omega) = 1 - |S_{11}(\omega)|^2 \tag{2.2}$$

Reflectance from the structure goes to zero at the frequency for which impedance of the structure is matched to the free space impedance (120π), and hence, absorptivity goes to unity. The proposed dual-band structure is optimized to get maximum absorptivity at the frequencies of absorption. The reflection and absorption characteristics of the proposed structure are presented in Figure 2.2. Maximum absorption of 95.02% and 99.84% are obtained at 4.215 GHz and 10.95 GHz with the full width at half maximum (FWHM) bandwidth of 0.194 GHz and 0.439 GHz, respectively for normal incidence of the wave. It is also observed that the identical absorption characteristics are obtained for the TE and TM polarization due to the symmetry of the structure in two orthogonal directions.

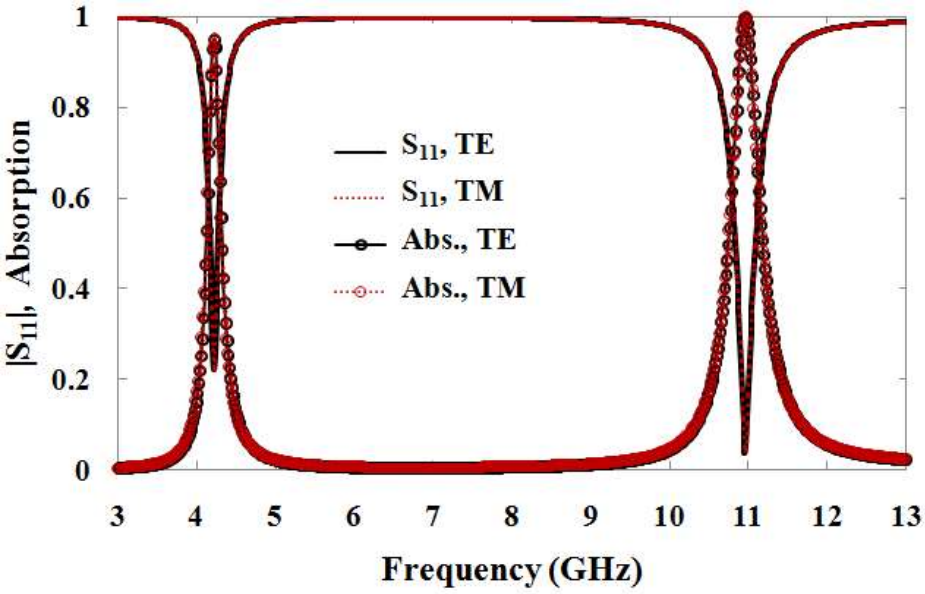

Figure 2.2: Reflection coefficient and absorption characteristics of the proposed structure.

2.2.3 Input Impedance

The general form of the normalized input impedance is as presented in Equation 2.3. At the frequency of absorption, *Im*(*Z*) undergo zero crossover. *Re*(*Z*) should be close to unity for perfect matching of the input impedance of the structure with free space impedance, so that reflection from the structure gets minimized and power of the incident wave completely absorb in the structure. The coupled power gets dissipated owing to the ohmic and dielectric losses of the structure. The normalized input impedance (*Z*) of the proposed structure is calculated using Equation 2.4 and is presented in Figure 2.3. In Equation 2.4, $|S_{21}| = 0$ is considered due to the complete metallic backplane on the bottom side of the substrate. The obtained values of normalized input impedance are 1.57− *j*0.04 and 1.07+*j*0.04 at 4.215 GHz and 10.95 GHz, respectively. It is observed that the *Re*(*Z*) of the structure at the first absorption frequency is higher than that of the free space impedance due to which significant

reflection loss occurs and absorptivity reduces by 4.98% at 4.215 GHz, however, at 10.95 GHz near-perfect absorption (~100%) is obtained.

$$Z = Re(Z) + jIm(Z) \tag{2.3}$$

$$Z = \sqrt{\frac{(1+S_{11})^2 - S_{21}^2}{(1-S_{11})^2 - S_{21}^2}} = \frac{1+S_{11}}{1-S_{11}} \tag{2.4}$$

2.3 Optimization of the Absorption Frequency and Absorption Level

2.3.1 Absorption Frequency

The absorption frequency is optimized by varying the geometrical parameters of the structure. The variation in the geometrical parameters changes the inductance (L) and capacitance (C) associated with the structure. The reflection response of the proposed unit cell under the variation of various geometrical parameters is presented in Figure 2.4(a)–(e). It is noted that at a time only one parameter is varying while all other parameters kept constant. It is observed from Figure 2.4(a) that increase in the cell

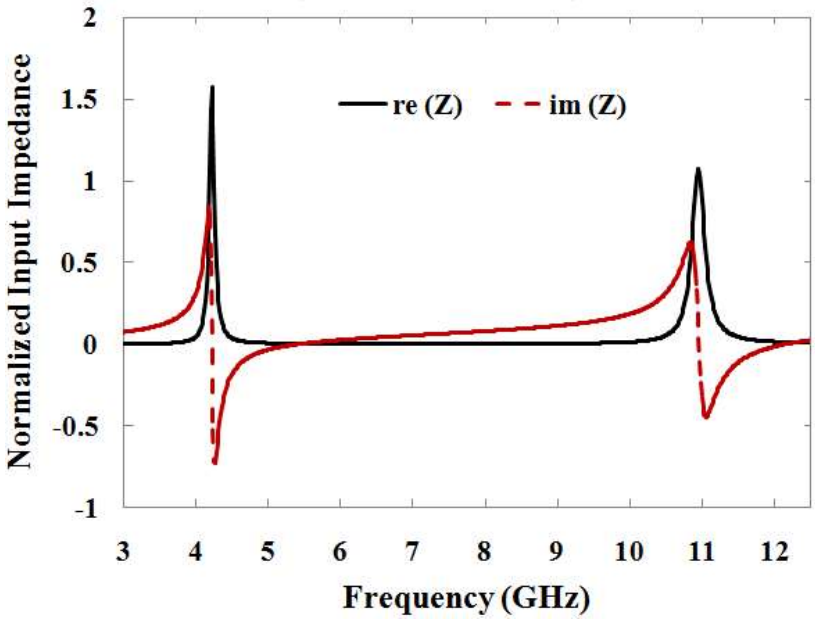

Figure 2.3: Normalized input impedance of the proposed structure.

periodicity 'p' brings both the absorption frequencies towards lower frequency side. With the increase in 'p', the length of CRR and diagonal arms increases, which increases the overall inductance of the structure and hence, resonant frequencies decreases. The increase in patch length 'l_p' increases the first absorption frequency (see Figure 2.4(b)). With the increase in patch length, diagonal arm length reduces which reduces the overall path of the surface current at first absorption frequency and hence frequency increases. It is further observed that increase in 'l_p' decreases the second absorption frequency and it is due to the increase in patch capacitance. Figure 2.4(c) and (d) shows that the increase in 'g_1' and 'w_d' shifts the first absorption frequency towards the higher frequency side keeping second absorption frequency almost constant. With the increase in 'g_1', CRR length reduces and the gap between two consecutive unit cell increases which reduces the associated inductance and capacitance, respectively. Therefore, the absorption frequency shifts towards higher frequency side. The increase in 'w_d' increases the width of the diagonal arm, which reduces the associated inductance and hence absorption frequency increases. The effect of varying CRR width 'w_c' is shown in Figure 2.4(e), and it is observed that increase in 'w_c' increases the second absorption frequency without significantly affecting the first absorption frequency. It is noted from the unit cell schematic that on increasing 'w_c' the diagonal arm length also reduces, which in turn reduces the associated inductance. At the first absorption frequency, the effect of the decrease in inductance is counterbalanced by the increase in capacitance due to the increase in width of the CRR. Therefore, the LC product remains same keeping first absorption frequency almost constant. Moreover, the reduction in inductance increases the second absorption frequency. It is further observed that the absorption level remains above 90% in almost all the cases. Hence, by suitably varying

these geometrical parameters, both the absorption frequencies can be tuned independently.

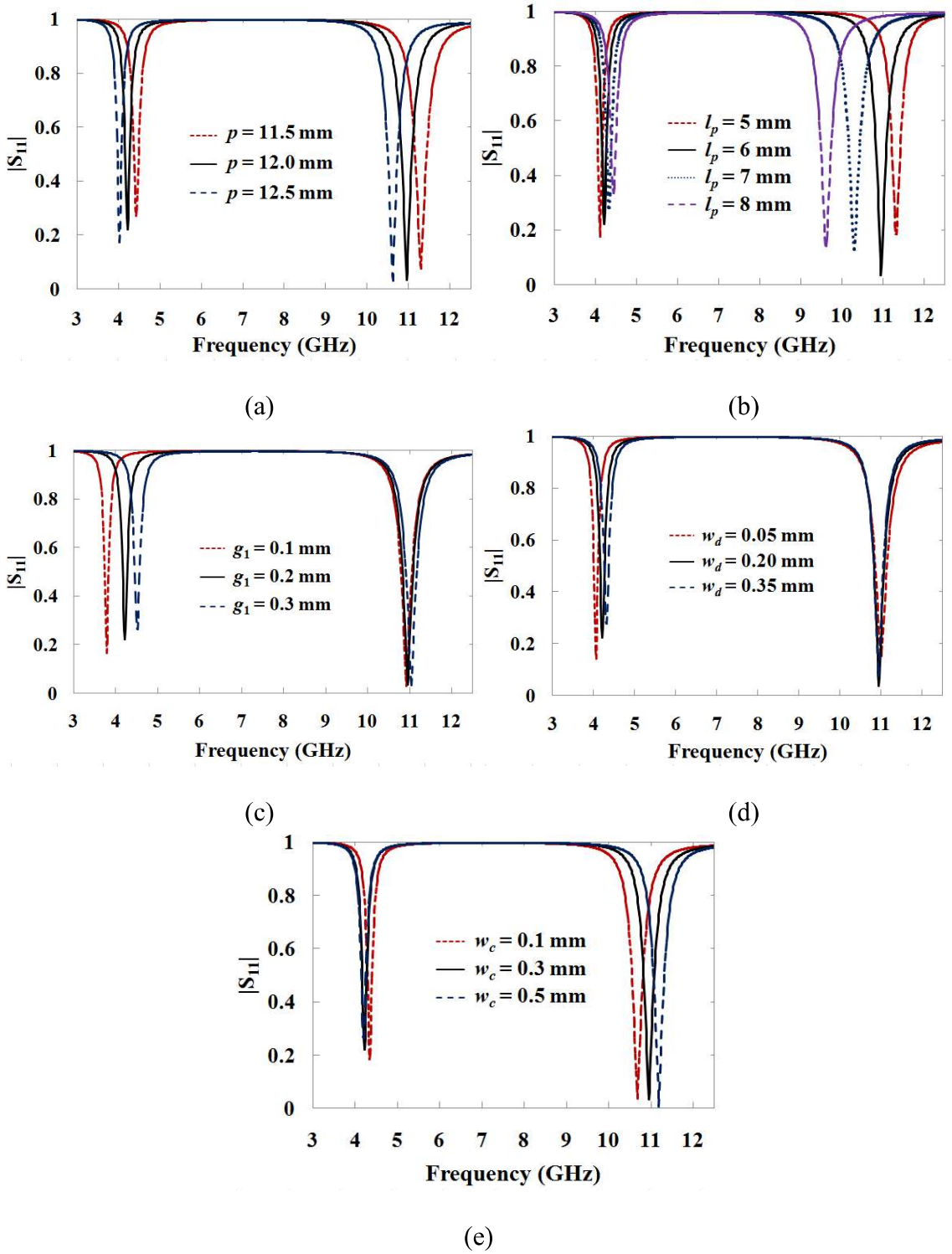

Figure 2.4: Effect of varying (a) 'p' (b) 'l_p' (c) 'g_1' (d) 'w_d' (e) 'w_c' on the reflection characteristics.

2.3.2 Absorption Level

At the frequency of absorption, $Im(Z)$ has zero crossover and the level of absorption is determined by the $Re(Z)$. $Re(Z)$ depends on the ohmic loss, dielectric loss, and the real part of the complex input impedance (Z_d) of the grounded lossy dielectric present in the structure. The $Re(Z_d)$ has a negligible effect on the absorption level [Costa *et al.* (2013)]. Figure 2.5 presents the simulated power loss density (volume) representing dielectric loss and surface power loss density representing the ohmic loss in the 90% absorption bands (4.191–4.240 GHz and 10.881–11.030 GHz). It is observed that the ohmic loss is about the fourth order of magnitude lower than that of the dielectric loss. Therefore, the effect of ohmic loss on the absorption level is neglected which is also consistent with the results presented in [Raynolds el al. (2003)]. Now, the dielectric loss is the only parameter which needs to be investigated for the in-depth analysis of the absorption level. The dielectric losses mainly depend on the thickness and the loss tangent of the dielectric material used.

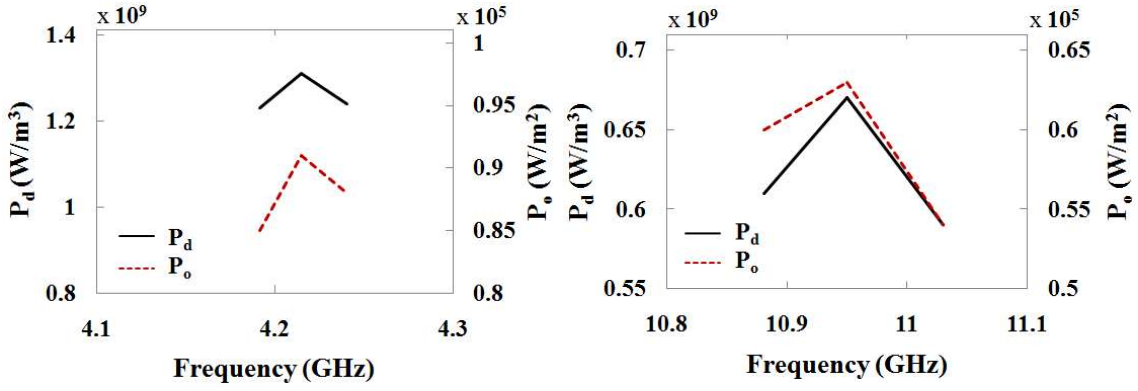

(a) (b)

Figure 2.5: Dielectric power loss density and surface power loss density for the (a) first absorption band and (b) second absorption band.

The thickness '*t*' of the substrate plays a dominant role in deciding the absorption level. It is observed from Figure 2.6(a) that the reflections from the structure first decreases with the increase of the '*t*' and then start increasing with further increase in '*t*'. Hence, there is always an optimum value of the thickness at which reflections becomes minimum for both the absorption frequencies. For its better understanding, the real part of the normalized input impedance (*Z*) of the structure is plotted against frequency for various substrate thickness in Figure 2.6(b). It is observed that the *Re*(*Z*) initially increases up to unity for $t = 0.6$ mm at first absorption frequency and for $t = 0.8$ mm at second absorption frequency and then *Re*(*Z*) go away from unity again. The optimization of the proposed structure is carried out with the substrate thickness of 0.8 mm owing to its availability. Furthermore, it is observed that the first absorption frequency decreases with the increase of '*t*' while second absorption frequency is almost unaffected. With the increase in substrate thickness capacitance decreases while associated inductance values increases. Since first absorption frequency is mainly due to the excitation of the CRR which has the high value of inductance owing to the smaller width and hence, increases in inductance is much greater in value compared to decrease in capacitance. Therefore, LC product increases effectively causing the frequency to shift to the lower side of the spectrum. The second absorption frequency is mainly determined by the excitation of the square patch and owing to the large width of the patch corresponding inductance value is smaller and comparable to the associated capacitance, and hence decrease in capacitance is counterbalanced by the increase in inductance keeping LC product almost constant.

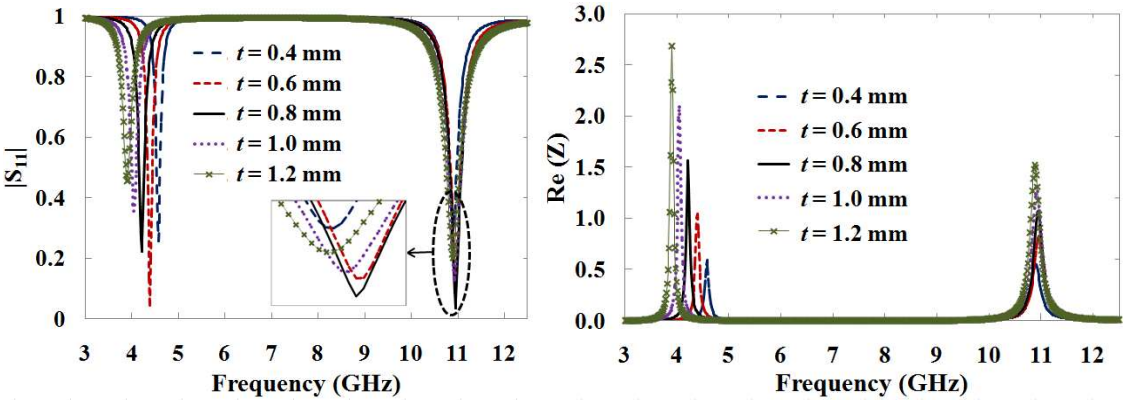

(a) (b)

Figure 2.6: Effect of varying substrate thickness '*t*' on the (a) reflection characteristics (see inset for the zoomed view of response at second absorption frequency) and (b) *Re*(*Z*) of the structure.

The variation in the dielectric loss tangent (*tanδ*) by keeping the real part of the permittivity constant does not affect the absorption frequency as shown in Figure 2.7(a). It is further observed from Figure 2.7(b) that the real part of the input impedance decreases with the increase of *tanδ*, and it becomes unity at a specific value of *tanδ* only.

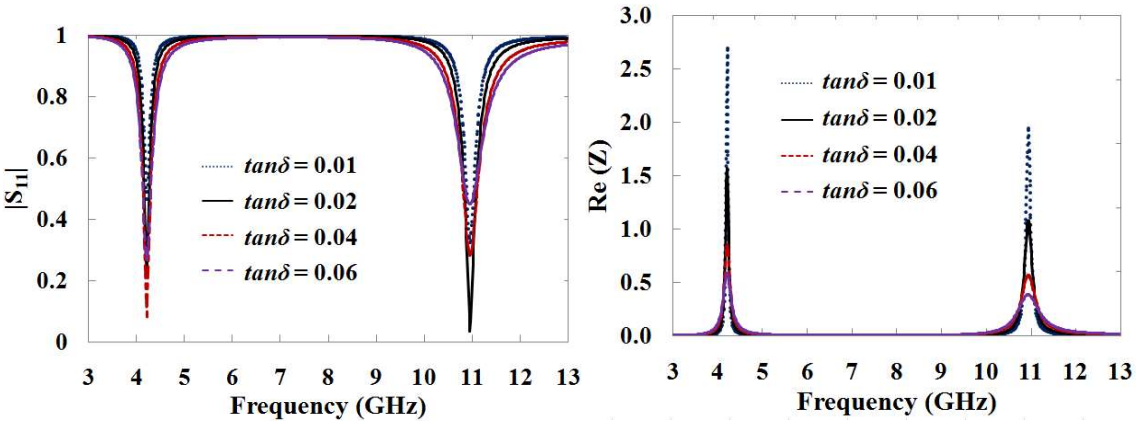

(a) (b)

Figure 2.7: Effect of varying dielectric loss tangent '*tanδ*' by keeping ε_r constant (ε_r = 4.4) on the (a) reflection characteristics, and (b) *Re*(*Z*) of the structure.

2.4 Absorption Mechanism

At the frequencies of absorption, reflection (due to perfect matching of structure impedance with free space impedance) and transmission (due to complete metallic backplane) become zero and hence the absorption of the structure become 100%. The coupling of the energy of the incident wave to the structure takes place due to the simultaneous excitation of electric and magnetic resonances in the structure.

The electric field distribution and surface current distribution for the TE polarized normally incident wave at the frequencies of absorption are presented in Figure 2.8 and 2.9, respectively. The plot in Figure 2.8 shows how the energy associated with the electrical component of incident wave transfers to the resonator at the absorption frequencies. The electrical energy is mainly confined to the loop and diagonal arms at the first absorption frequency while in the patch and diagonal arms at the second absorption frequency. Figure 2.9 presents the surface current at the top and bottom metallic layers and it is observed that the current in the two layers is anti-parallel. Therefore, current loops are formed in between the two layers in a direction perpendicular to the incident magnetic field. This leads to the generation of magnetic resonance and energy associated with the incident magnetic field couples to the structure.

2.5 Polarization-insensitive Behaviour

To investigate the polarization sensitivity of the proposed structure, the plane containing the *E*-*H* vector of the incident wave is rotated from 0^0 to 45^0 (response for the above angles will remain same owing to the diagonal symmetry in the structure), and the reflection response is presented in Figure 2.10. The proposed structure is polarization insensitive as the identical response is observed for the variation in polarization angle 'ϕ'.

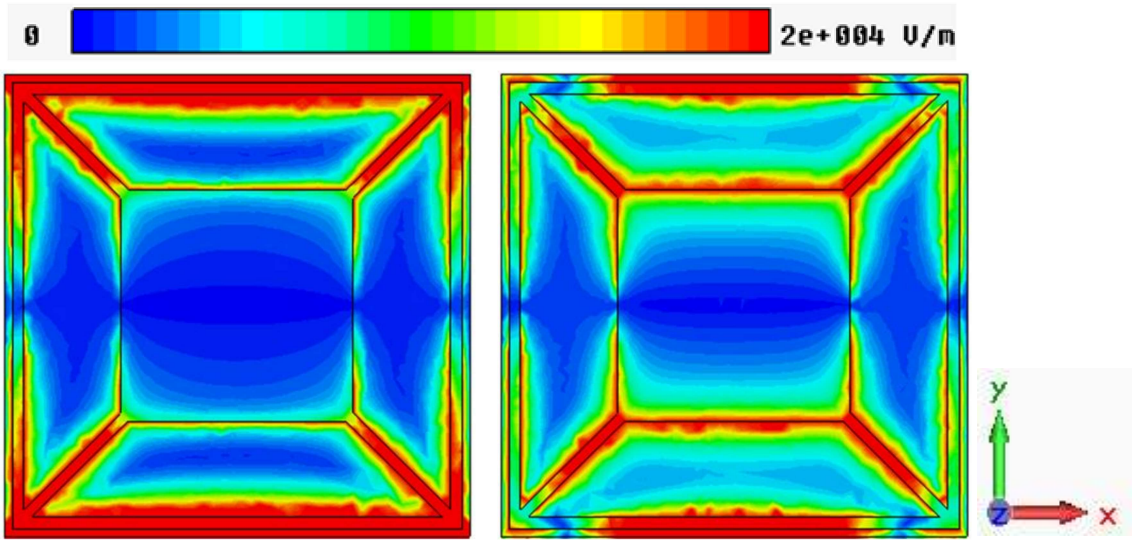

4.215 GHz *10.95 GHz*

Figure 2.8: *E*-field distributions at the peak absorption frequencies.

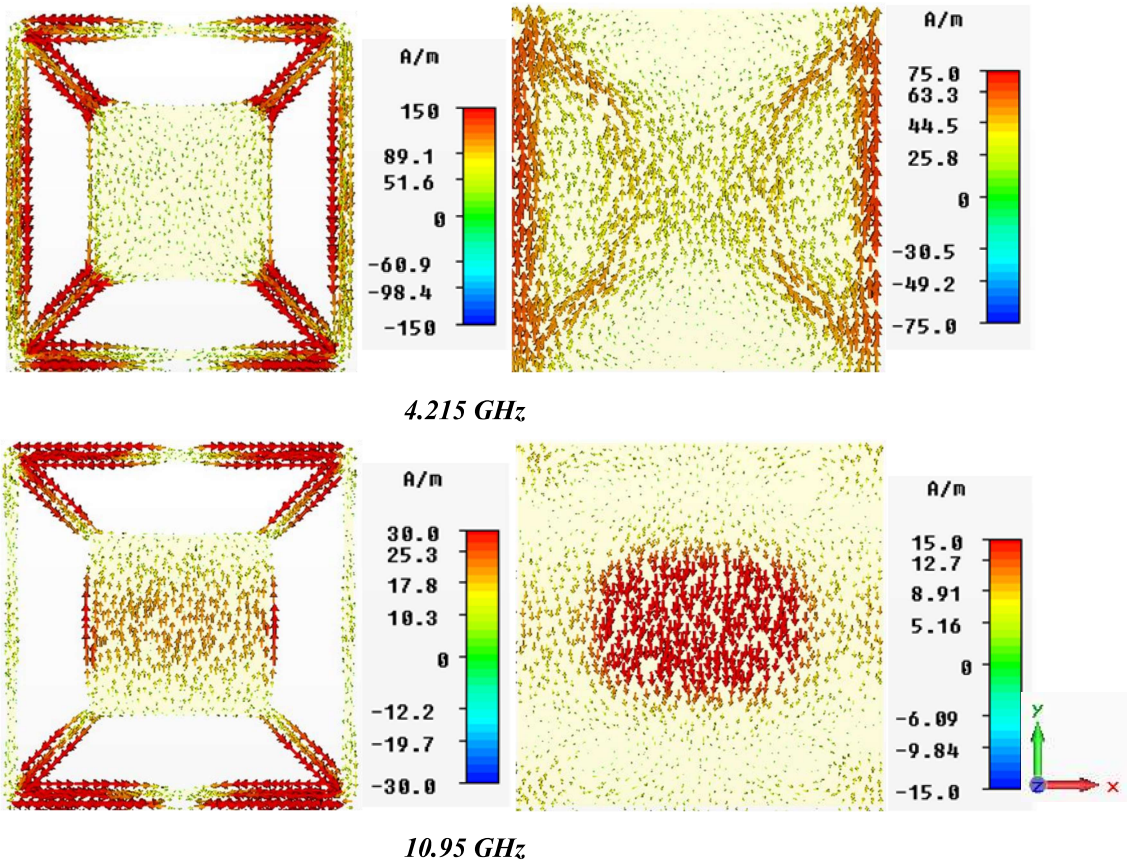

4.215 GHz

10.95 GHz

Figure 2.9: Surface current distributions on the top and bottom layers of the proposed absorber at the peak absorption frequencies.

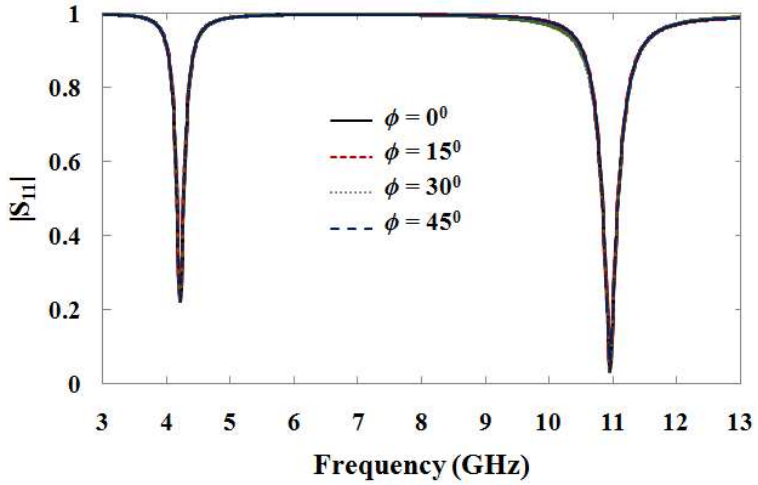

Figure 2.10: Simulated reflection response under the variation of polarization angle 'ϕ'.

2.6 Constitutive Parameter Retrieval

Owing to the very small thickness ($t << \lambda$) of the proposed absorber, it would be better to treat it as a metasurface [Hollaway *et al.* (2012)]. The characterization of such surfaces in terms of surface susceptibilities is the more appropriate approach compared to its characterization in terms of bulk effective material properties [Hollaway *et al.* (2011)]. Moreover, this approach provides straightforward dependence of electrical surface susceptibilities (χ_{es}) and magnetic surface susceptibilities (χ_{ms}) on the S_{11} of the structure as in Equation 2.5. The effective permittivity (ε_{eff}) and permeability (μ_{eff}) of the structure of thickness 't' are calculated from χ_{es} and χ_{ms} as given in Equation 2.6.

$$\chi_{es} = \frac{2j}{k_0}\frac{S_{11}-1}{S_{11}+1}, \qquad \chi_{ms} = \frac{2j}{k_0}\frac{S_{11}+1}{S_{11}-1}. \tag{2.5}$$

$$\varepsilon_{eff} = 1+\frac{\chi_{es}}{t}, \qquad \mu_{eff} = 1+\frac{\chi_{ms}}{t}. \tag{2.6}$$

where, k_0 is wave-number of the free space.

As discussed earlier that the normalized input impedance (Z) of the structure should be unity for perfect absorption. The relation of the intrinsic impedance ($Z(\omega)$) of the structure with its permittivity and permeability is given in Equation 2.7. Therefore, the real and imaginary parts of ε_{eff} and μ_{eff} should be equal separately for getting perfect absorption.

$$Z(\omega) = \sqrt{\frac{\mu(\omega)}{\varepsilon(\omega)}} \tag{2.7}$$

where,

$$\mu(\omega) = \mu'(\omega) - j\mu''(\omega),$$
$$\varepsilon(\omega) = \varepsilon'(\omega) - j\varepsilon''(\omega).$$

The frequency response of the extracted real part of ε_{eff} and μ_{eff} and imaginary part of ε_{eff} and μ_{eff} considering the normal incidence of the wave are presented in Figure 2.11(a) and (b), respectively, and their values corresponding to the two peak absorption frequencies are reported in Table 2.1. It is observed that the difference in real part of ε_{eff} and μ_{eff} and imaginary part of ε_{eff} and μ_{eff} at 4.215 GHz are more pronounced compared to the difference at 10.95 GHz. Hence, the extracted values further justify the low absorption at first absorption frequency compared to second absorption frequency.

The procedure adopted for the effective parameter retrieval presented here is efficient and correct for the structures like metamaterial absorber with metallic backplane as the adopted method only relies on S_{11} of the structure. The used procedure has already been validated in the literature [Bhattacharyya and Srivastava (2014)].

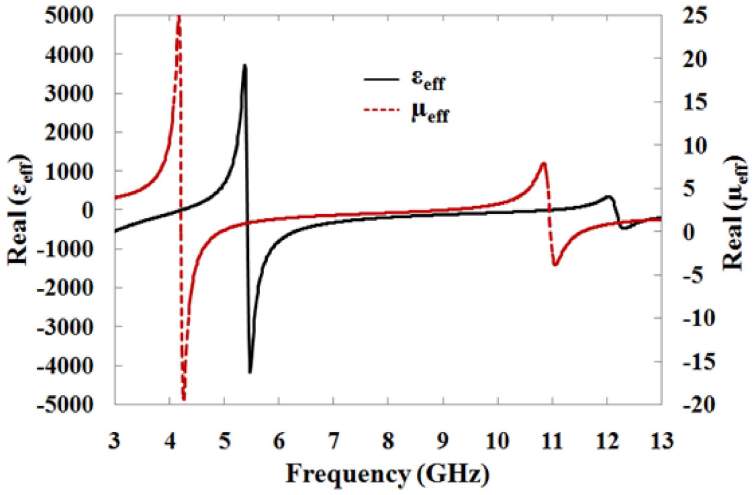

(a)

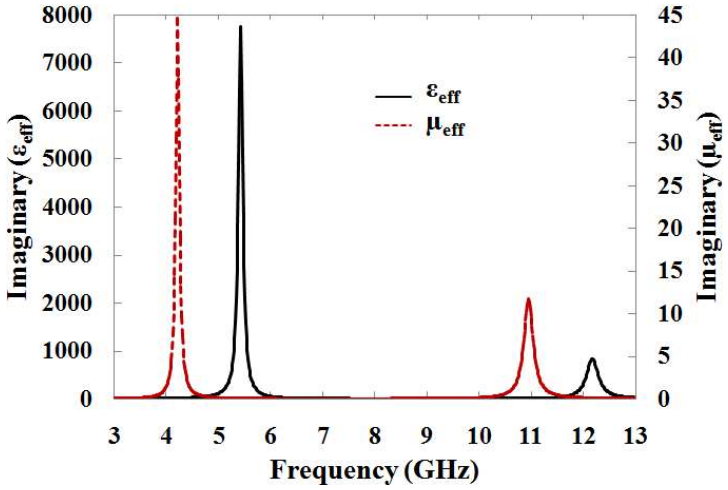

(b)

Figure 2.11: Extracted constitutive parameters of the proposed structure, (a) real part of ε_{eff} and μ_{eff}, and (b) imaginary part of ε_{eff} and μ_{eff}.

Table 2.1. Constitutive Parameters of the Proposed Structure at the Peak Absorption Frequencies

Frequency	Real (ε_{eff})	Real (μ_{eff})	Imaginary (ε_{eff})	Imaginary (μ_{eff})
4.215 GHz	1.48	-0.19	17.99	44.52
10.95 GHz	0.66	1.40	10.14	11.69

2.7 Experimental Results

An array of 216 x 216 mm^2 (18 x 18 unit cells) of the proposed absorber is fabricated. Free space measurement method is employed for the measurement of the reflection response of the fabricated sample. Since the absorption response lies in C-band (4.215 GHz) and X-band (10.95 GHz), two pairs of C- and X- band horn antennas are used as transmitting and receiving antennas. The horn antennas are connected to the Anritsu's vector network analyzer MS2038C to measure S_{21}. The sample is placed at a distance calculated from Fraunhofer far field criteria. The measured S_{21} at the transmitting end become S_{11} as observed from the sample side. The experimental setup in the anechoic chamber is shown in Figure 2.12. To avoid any unwanted effect of the imperfections due to surrounding and edges/corners of the sample, the reflection from the sample are normalized with the reflection from the copper sheet of identical dimensions.

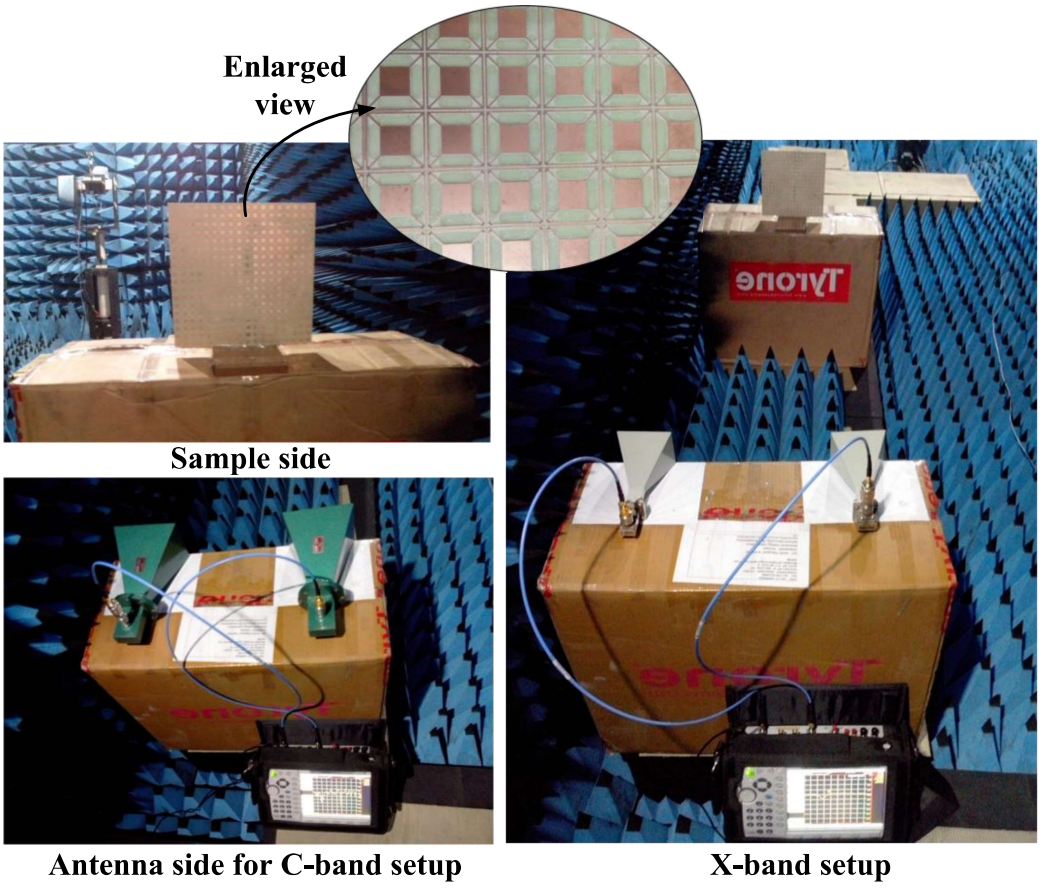

Figure 2.12: Experimental setup.

2.7.1 Normal Incidence

The measured and simulated reflection responses of the proposed absorber for normally incident wave are compared in Figure 2.13. The measured absorptivities of 91.30% and 98.80% are obtained at 4.224 GHz and 10.94 GHz, respectively. The obtained measured response is pretty close to the simulated response. The slight discrepancy in the results is due to the finite size of the fabricated sample and the fabrication tolerance of the structure. It is also observed that the measured response remains identical when we rotate the *E*-plane of both the transmitting and receiving horn antennas by 90^0 to realize TM polarized incident wave.

2.7.2 Oblique Incidence

The wide angle performance of the proposed structure is investigated for the TE and TM polarized incident wave by varying the angle of incidence 'θ'. For TE polarized case, the plane containing the propagation vector (k) and H-vector is rotated by the incidence angle 'θ' keeping the direction of E-vector constant. For TM polarized case, the k-E plane is rotated by the incidence angle 'θ' keeping the direction of H-vector

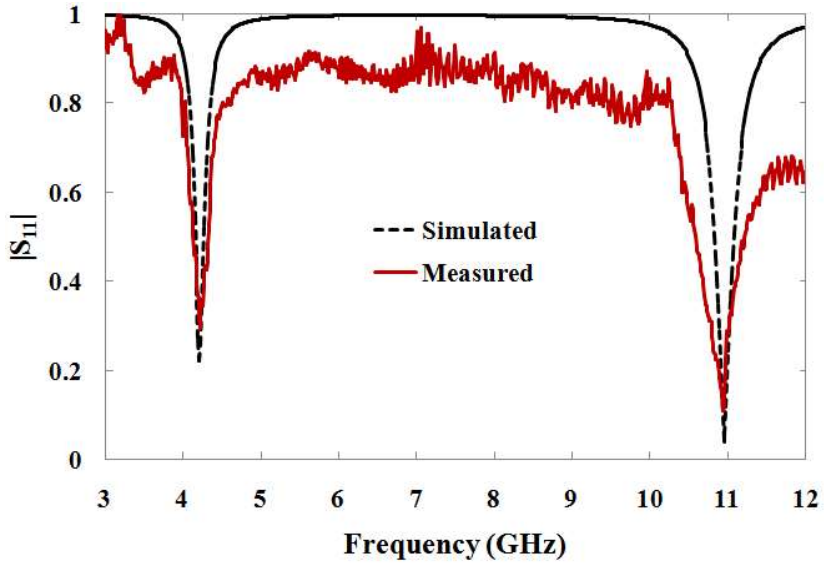

Figure 2.13: Measured and simulated reflection response for normally incident wave.

constant. The measured response is obtained by turning both the horn antennas by an angle 'θ'. The simulated and measured responses with an oblique incidence of 15^0, 30^0, 45^0, and 60^0 are shown in Figure 2.14(a)–(d). It is observed from the simulated results that the two absorption frequencies remain almost the same (with a variation of less than 5%) for the TE and TM polarized incidence wave with varying incidence angle. However, the absorptivity (calculated using Equation 2.1) decreases beyond a certain value of 'θ'. For TE polarized incident wave, absorptivity is better than 95% up to 60^0 and better than 96% up to 45^0 for the first and second absorption frequency, respectively. For TM polarized incident wave, absorptivity is better than 92% up to 45^0 and better than 99% up to 60^0 for the first and second absorption frequency, respectively. Thus, the proposed absorber meets the requirement of wide angle performance. It is also observed that the measured responses at various angles of incidence are in close agreement to the simulated responses. The discrepancy in the measured and simulated reflection response increases with the incidence angle 'θ' and it is due to the imperfection in the placement of standard horn antennas tilted at an angle 'θ' during the experiment.

A secondary resonance is observed for $\theta > 0^0$ around 8.1 GHz and 8.5 GHz for the TE and TM polarized case, respectively. The *H*- and *E*- fields become inclined at an angle 'θ' for the TE and TM polarized oblique incident waves, respectively. The horizontal and vertical components of the inclined fields generate primary and secondary resonances, respectively. The horizontal component decreases with angle 'θ', and so the accumulated charge, and hence the absorption decreases with angle 'θ'. While vertical component increases with angle 'θ', and so the accumulated charge, and hence absorption increases with angle 'θ'. However, improper impedance matching is observed at the secondary resonance.

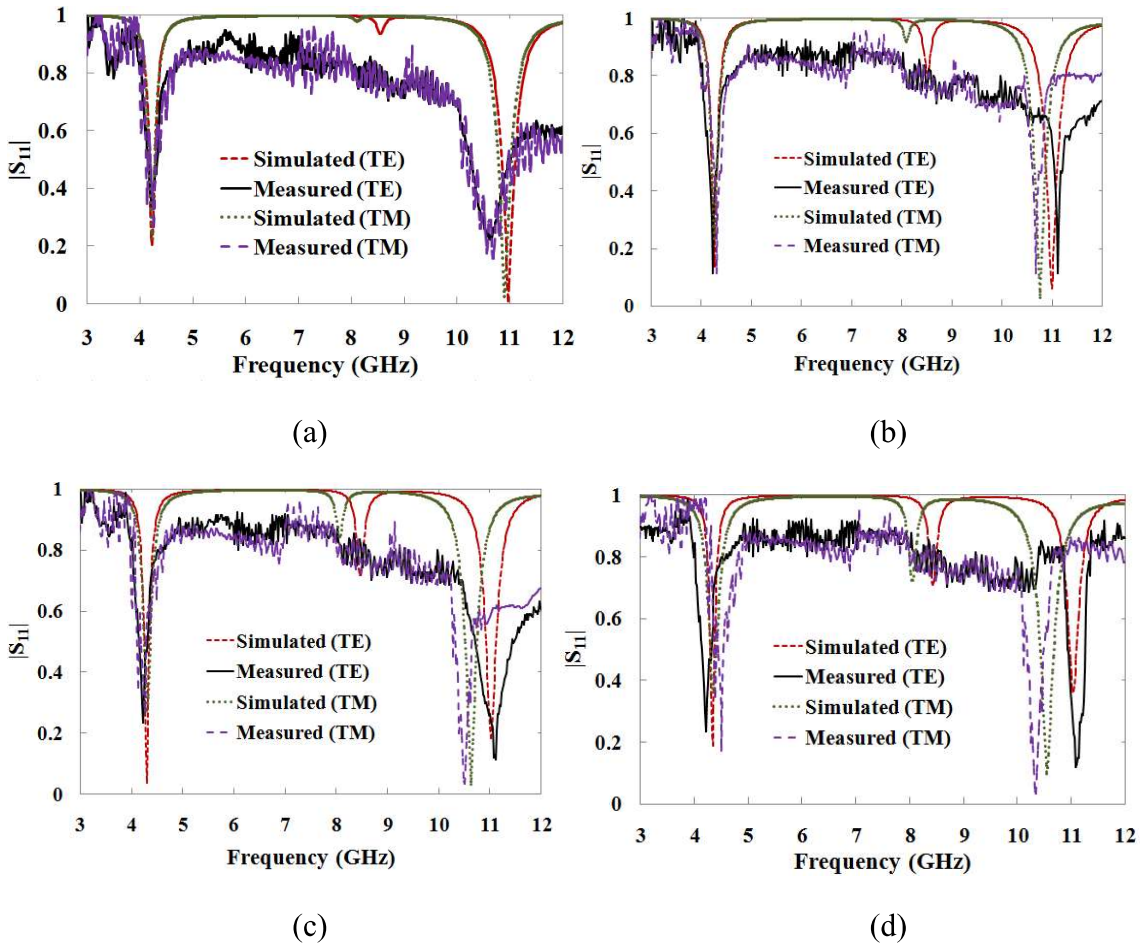

Figure 2.14: Measured and simulated reflection response for oblique incidence of (a) 15^0 (b) 30^0 (c) 45^0 (d) 60^0.

2.8 Performance Comparison with Some Other Dual-band Absorbers

The comparison of the proposed absorber unit cell is presented in Table 2.2 with some other dual-band absorber structures reported in the literature. The comparison is done in terms of unit cell periodicity and thickness. It is observed that proposed absorber is compact and ultra-thin compared to the other absorbers. It is also observed that the relative bandwidth of the proposed absorber is comparable to the other absorbers.

Table 2.2: Performance Comparison

Reference	**Peak absorption frequency and peak absorptivity**	**Relative bandwidth**	**Unit cell periodicity**	**Unit cell thickness**
[Li *et al.* (2010)]	11.15 GHz (97%) and 16.01 GHz (99%)	2.87% and 3.87%	12 mm (0.446λ)	0.5 mm (0.019λ)
[Baskey and Akhtar (2013)]	6.10 GHz (98.5%) and 10 GHz (99.7%)	1.97% and 1.40%	12 mm (0.244λ)	1 mm (0.020λ)
[Dincer *et al.* (2013)]	4.0 GHz (99%) and 5.6 GHz (84%)	4.75% and 3.25%	25 mm (0.333λ)	1.6 mm (0.021λ)
[Ayop *et al.* (2014)a]	9 GHz (97.00%) and 10 GHz (97.77%)	3.59% and 3.31%.	18 mm (0.540λ)	0.8 mm (0.024λ)
[Jamilan *et al.* (2014)]	5.6 GHz (97%) and 6 GHz (99%)	Not Reported	20 mm (0.373λ)	1.5 mm (0.028λ)
[Zhang *et al.* (2014)]	4.29 GHz (98.6%) and 6.49 GHz (99.8%)	Not Reported	21.8 mm (0.312λ)	0.5 mm (0.007λ)
[Dincer *et al.* (2014)]	4.42 GHz (95.6%) and 5.62 GHz (99.9%)	7.47% and 3.56%	19.9 mm (0.293λ)	1.6 mm (0.024λ)
Proposed	4.215 GHz (95.02%) and 10.95 GHz (99.84%)	4.60% and 4.01%	12 mm (0.169λ)	0.8 mm (0.011λ)

where λ corresponds to the lowest peak absorption frequency.

2.9 Conclusion

In this chapter, a compact, ultra-thin absorber unit cell with dual-band absorption response has been presented. The structure was analyzed parametrically and its absorption mechanism was explained. The proposed structure was polarization

insensitive and has wide angle performance for both the TE and TM polarized incident wave. Constitutive electromagnetic parameters of the structure were extracted to get an insight into the absorption phenomenon. The experimental results of the proposed absorber were found in close agreement to the simulated results.

To get a good insight into the resonance phenomenon, the equivalent circuit modeling of the proposed absorber is needed. A transmission line model (TLM) is developed for the proposed absorber and the values of lumped parameters and coupling capacitances are calculated in the next chapter.